Simscape Model - Nano Active Stabilization System

Dehaeze Thomas

February 18, 2025

Contents

1 Introduction **3**

2 Control Kinematics **4**
2.1 Micro Station Kinematics 4
2.2 Computation of the sample's pose error 5
2.3 Position error in the frame of the struts 5
2.4 Control Architecture - Summary 6

3 Decentralized Active Damping **7**
3.1 IFF Plant 7
3.2 Controller Design 7

4 Centralized Active Vibration Control **10**
4.1 HAC Plant 10
4.2 Effect of Nano-Hexapod Stiffness on System Dynamics 13
4.3 Controller design 13
4.4 Tomography experiment 14

Bibliography **17**

1 Introduction

The preceding chapters have established crucial foundational elements for the development of the Nano Active Stabilization System (NASS). The uniaxial model study demonstrated that very stiff nano-hexapod configurations should be avoided due to their high coupling with the micro-station's dynamics. A rotating three-degree-of-freedom model revealed that soft nano-hexapod designs prove unsuitable for rotating applications due to gyroscopic effect. To further improve the model accuracy, a multi-body model of the micro-station was developed, which was carefully tuned using experimental modal analysis. Furthermore, a multi-body model of the nano-hexapod was created, that can then be seamlessly integrated with the micro-station model, as illustrated in Figure 1.1.

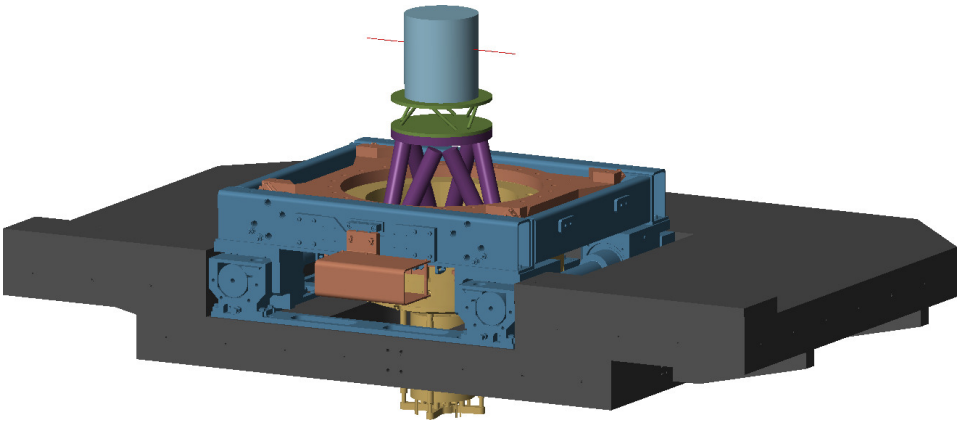

Figure 1.1: 3D view of the NASS multi-body model

Building upon these foundations, this chapter presents the validation of the NASS concept. The investigation begins with the previously established nano-hexapod model, with actuator stiffness $k_a = 1\,N/\mu m$. A thorough examination of the control kinematics is presented in Section 2, detailing how both external metrology and nano-hexapod internal sensors are utilized in the control architecture. The control strategy is then implemented in two steps: first, the decentralized IFF is used for active damping (Section 3), then a High Authority Control is develop to stabilize the sample's position in a large bandwidth (Section 4).

The robustness of the proposed control scheme is rigorously evaluated across various operational conditions. Particular attention is paid to system performance under changing payload masses and varying spindle rotational velocities, as these represent critical operational parameters in practical applications.

This chapter marks the conclusion of the conceptual design phase, with simulation of tomography experiments providing strong evidence for the viability of the proposed NASS architecture. The findings presented here establish a solid foundation for subsequent detailed design and experimental validation phases.

2 Control Kinematics

Figure 2.1 presents a schematic overview of the NASS. This section focuses specifically on the components of the "Instrumentation and Real-Time Control" block.

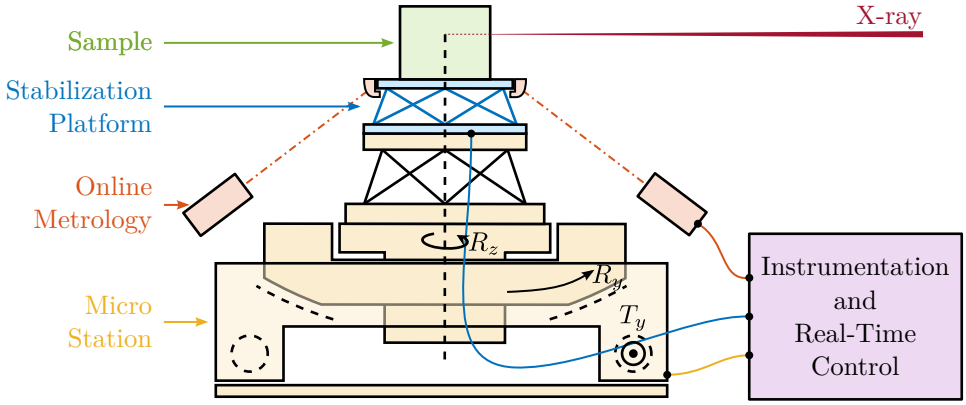

Figure 2.1: Schematic of the Nano Active Stabilization System

As established in the previous section on Stewart platforms, the proposed control strategy combines Decentralized Integral Force Feedback with a High Authority Controller performed in the frame of the struts.

For the Nano Active Stabilization System, computing the positioning errors in the frame of the struts involves three key steps. First, the system computes the desired sample pose relative to a frame representing the point where the X-ray light is focused using micro-station kinematics, as detailed in Section 2.1. Second, it measures the actual sample pose relative to the same fix frame, described in Section 2.2. Finally, it determines the sample pose error and maps these errors to the nano-hexapod struts, as explained in Section 2.3.

The complete control architecture is detailed in Section 2.4.

2.1 Micro Station Kinematics

The micro-station kinematics enables the computation of the desired sample pose from the reference signals of each micro-station stage. These reference signals consist of the desired lateral position r_{D_y}, tilt angle r_{R_y}, and spindle angle r_{R_z}. The micro-hexapod pose is defined by six parameters: three translations $(r_{D_{\mu x}}, r_{D_{\mu y}}, r_{D_{\mu z}})$ and three rotations $(r_{\theta_{\mu x}}, r_{\theta_{\mu y}}, r_{\theta_{\mu z}})$.

Using these reference signals, the desired sample position relative to the fixed frame is expressed through the homogeneous transformation matrix $\boldsymbol{T}_{\mu\text{-station}}$, as defined in equation (2.1).

$$\boldsymbol{T}_{\mu\text{-station}} = \boldsymbol{T}_{D_y} \cdot \boldsymbol{T}_{R_y} \cdot \boldsymbol{T}_{R_z} \cdot \boldsymbol{T}_{\mu\text{-hexapod}} \tag{2.1}$$

$$\begin{aligned}
\boldsymbol{T}_{D_y} &= \begin{bmatrix} 1 & 0 & 0 & 0 \\ 0 & 1 & 0 & r_{D_y} \\ 0 & 0 & 1 & 0 \\ 0 & 0 & 0 & 1 \end{bmatrix} \quad \boldsymbol{T}_{\mu\text{-hexapod}} = \left[\begin{array}{ccc|c} \multicolumn{3}{c|}{\boldsymbol{R}_x(r_{\theta_{\mu x}})\boldsymbol{R}_y(r_{\theta_{\mu y}})\boldsymbol{R}_z(r_{\theta_{\mu z}})} & \begin{matrix} r_{D_{\mu x}} \\ r_{D_{\mu y}} \\ r_{D_{\mu z}} \end{matrix} \\ \hline 0 & 0 & 0 & 1 \end{array}\right] \\
\boldsymbol{T}_{R_z} &= \begin{bmatrix} \cos(r_{R_z}) & -\sin(r_{R_z}) & 0 & 0 \\ \sin(r_{R_z}) & \cos(r_{R_z}) & 0 & 0 \\ 0 & 0 & 1 & 0 \\ 0 & 0 & 0 & 1 \end{bmatrix} \quad \boldsymbol{T}_{R_y} = \begin{bmatrix} \cos(r_{R_y}) & 0 & \sin(r_{R_y}) & 0 \\ 0 & 1 & 0 & 0 \\ -\sin(r_{R_y}) & 0 & \cos(r_{R_y}) & 0 \\ 0 & 0 & 0 & 1 \end{bmatrix}
\end{aligned} \tag{2.2}$$

2.2 Computation of the sample's pose error

The external metrology system measures the sample position relative to the fixed granite. Due to the system's symmetry, this metrology provides measurements for five degrees of freedom: three translations (D_x, D_y, D_z) and two rotations (R_x, R_y).

The sixth degree of freedom (R_z) is still required to compute the errors in the frame of the nano-hexapod struts (i.e. to compute the nano-hexapod inverse kinematics). This R_z rotation is estimated by combining measurements from the spindle encoder and the nano-hexapod's internal metrology, which consists of relative motion sensors in each strut (note that the micro-hexapod is not used for R_z rotation, and is therefore ignore for R_z estimation).

The measured sample pose is represented by the homogeneous transformation matrix $\boldsymbol{T}_{\text{sample}}$, as shown in equation (2.3).

$$\boldsymbol{T}_{\text{sample}} = \left[\begin{array}{ccc|c} \multicolumn{3}{c|}{\boldsymbol{R}_x(R_x)\boldsymbol{R}_y(R_y)\boldsymbol{R}_z(R_z)} & \begin{matrix} D_x \\ D_y \\ D_z \end{matrix} \\ \hline 0 & 0 & 0 & 1 \end{array}\right] \tag{2.3}$$

2.3 Position error in the frame of the struts

The homogeneous transformation formalism enables straightforward computation of the sample position error. This computation involves the previously computed homogeneous 4×4 matrices: $\boldsymbol{T}_{\mu\text{-station}}$ representing the desired pose, and $\boldsymbol{T}_{\text{sample}}$ representing the measured pose. Their combination yields $\boldsymbol{T}_{\text{error}}$, which expresses the position error of the sample in the frame of the rotating nano-hexapod, as shown in equation (2.4).

$$\boldsymbol{T}_{\text{error}} = \boldsymbol{T}_{\mu\text{-station}}^{-1} \cdot \boldsymbol{T}_{\text{sample}} \tag{2.4}$$

The known structure of the homogeneous transformation matrix facilitates efficient real-time computation of the inverse. From $\boldsymbol{T}_{\text{error}}$, the position and orientation errors $\boldsymbol{\epsilon}_{\mathcal{X}} = [\epsilon_{D_x},\ \epsilon_{D_y},\ \epsilon_{D_z},\ \epsilon_{R_x},\ \epsilon_{R_y},\ \epsilon_{R_z}]$ of the sample are extracted using equation (2.5):

$$
\begin{aligned}
\epsilon_{D_x} &= \boldsymbol{T}_{\text{error}}(1,4) \\
\epsilon_{D_y} &= \boldsymbol{T}_{\text{error}}(2,4) \\
\epsilon_{D_z} &= \boldsymbol{T}_{\text{error}}(3,4) \\
\epsilon_{R_y} &= \text{atan2}(\boldsymbol{T}_{\text{error}}(1,3), \sqrt{\boldsymbol{T}_{\text{error}}(1,1)^2 + \boldsymbol{T}_{\text{error}}(1,2)^2}) \\
\epsilon_{R_x} &= \text{atan2}(-\boldsymbol{T}_{\text{error}}(2,3)/\cos(\epsilon_{R_y}), \boldsymbol{T}_{\text{error}}(3,3)/\cos(\epsilon_{R_y})) \\
\epsilon_{R_z} &= \text{atan2}(-\boldsymbol{T}_{\text{error}}(1,2)/\cos(\epsilon_{R_y}), \boldsymbol{T}_{\text{error}}(1,1)/\cos(\epsilon_{R_y}))
\end{aligned}
\tag{2.5}
$$

Finally, these errors are mapped to the strut space through the nano-hexapod Jacobian matrix (2.6).

$$
\boldsymbol{\epsilon}_{\mathcal{L}} = \boldsymbol{J} \cdot \boldsymbol{\epsilon}_{\mathcal{X}} \tag{2.6}
$$

2.4 Control Architecture - Summary

The complete control architecture is summarized in Figure 2.2. The sample pose is measured using external metrology for five degrees of freedom, while the sixth degree of freedom (Rz) is estimated by combining measurements from the nano-hexapod encoders and spindle encoder.

The sample reference pose is determined by the reference signals of the translation stage, tilt stage, spindle, and micro-hexapod. Position error computation follows a two-step process: first, homogeneous transformation matrices are used to determine the error in the nano-hexapod frame, then the Jacobian matrix $\boldsymbol{J}$ maps these errors to individual strut coordinates.

For control purposes, force sensors mounted on each strut are used in a decentralized way for active damping, as detailed in Section 3. Then, the high authority controller uses the computed errors in the frame of the struts to provides real-time stabilization of the sample position (Section 4).

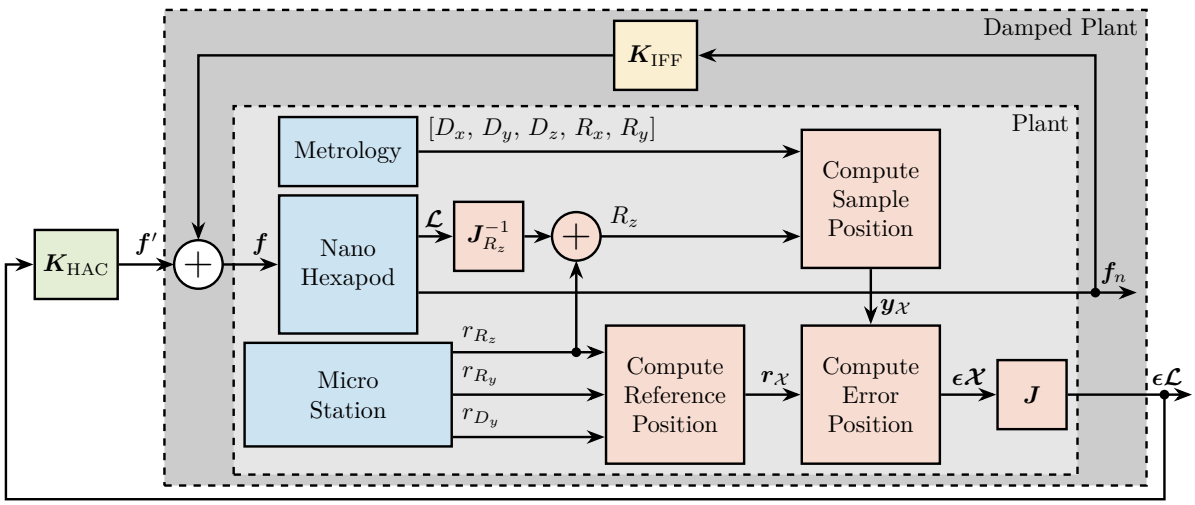

Figure 2.2: Control architecture for the NASS. Physical systems are shown in blue, control kinematics elements in red, decentralized Integral Force Feedback controller in yellow and centralized High Authority controller in green.

3 Decentralized Active Damping

Building upon the uniaxial model study, this section implements decentralized Integral Force Feedback (IFF) as the first component of the HAC-LAC strategy. Springs in parallel to the force sensors are used to guarantee the control robustness as was found using the 3DoF rotating model. The objective here is to design a decentralized IFF controller that provides good damping of the nano-hexapod modes across payload masses ranging from 1 to 50 kg and rotational velocity up to 360 deg/s. Used payloads have a cylindrical shape with 250 mm height and with masses of 1 kg, 25 kg, and 50 kg.

3.1 IFF Plant

Transfer functions from actuator forces f_i to force sensor measurements f_{mi} are computed using the multi-body model. Figure 3.1 examines how parallel stiffness affects the plant dynamics, with identification performed at maximum spindle velocity $\Omega_z = 360\,\text{deg/s}$ and with a payload mass of 25 kg.

Without parallel stiffness (Figure 3.1a), the dynamics exhibits non-minimum phase zeros at low frequency, confirming predictions from the three-degree-of-freedom rotating model. Adding parallel stiffness (Figure 3.1b) transforms these into minimum phase complex conjugate zeros, enabling unconditionally stable decentralized IFF implementation.

Though both cases show significant coupling around resonances, stability is guaranteed by the collocated arrangement of actuators and sensors [1].

The effect of rotation, shown in Figure 3.2a, is negligible as the actuator stiffness ($k_a = 1\,N/\mu m$) is large compared to the negative stiffness induced by gyroscopic effects (estimated from the 3DoF rotating model).

Figure 3.2b illustrate the effect of payload mass on the plant dynamics. While the poles and zeros are shifting with payload mass, the alternating pattern of poles and zeros is maintained, ensuring that the phase remains bounded between 0 and 180 degrees, and thus good robustness properties.

3.2 Controller Design

Previous analysis using the 3DoF rotating model showed that decentralized Integral Force Feedback (IFF) with pure integrators is unstable due to gyroscopic effects caused by spindle rotation. This finding is also confirmed with the multi-body model of the NASS: the system is unstable when using pure integrators and without parallel stiffness.

This instability can be mitigated by introducing sufficient stiffness in parallel with the force sensors. However, as illustrated in Figure 3.1b, adding parallel stiffness increases the low frequency gain. If

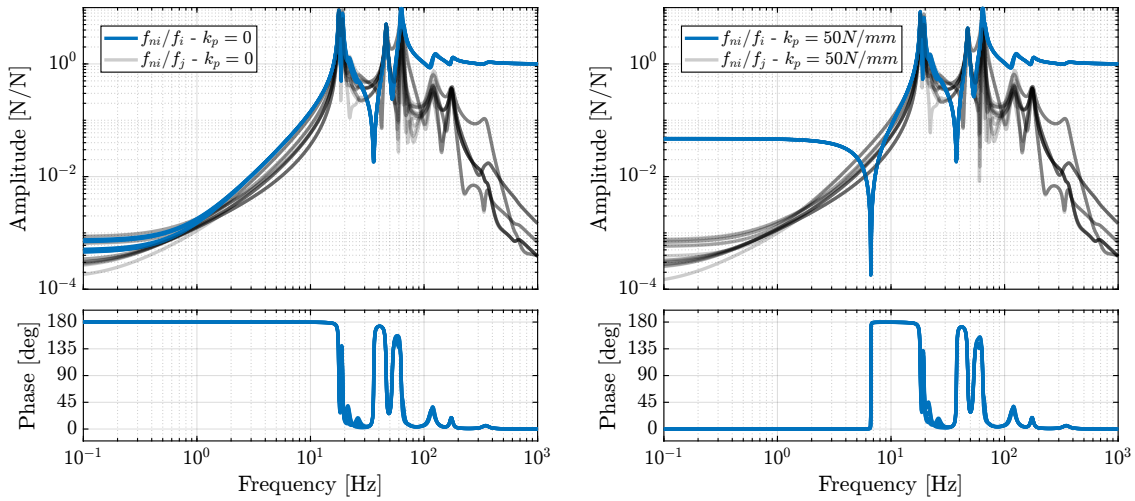

(a) without parallel stiffness

(b) with parallel stiffness

Figure 3.1: Effect of stiffness parallel to the force sensor on the IFF plant with $\Omega_z = 360\,\text{deg/s}$ and payload mass of 25kg. The dynamics without parallel stiffness has non-minimum phase zeros at low frequency (a). The added parallel stiffness transforms the non-minimum phase zeros to complex conjugate zeros (b)

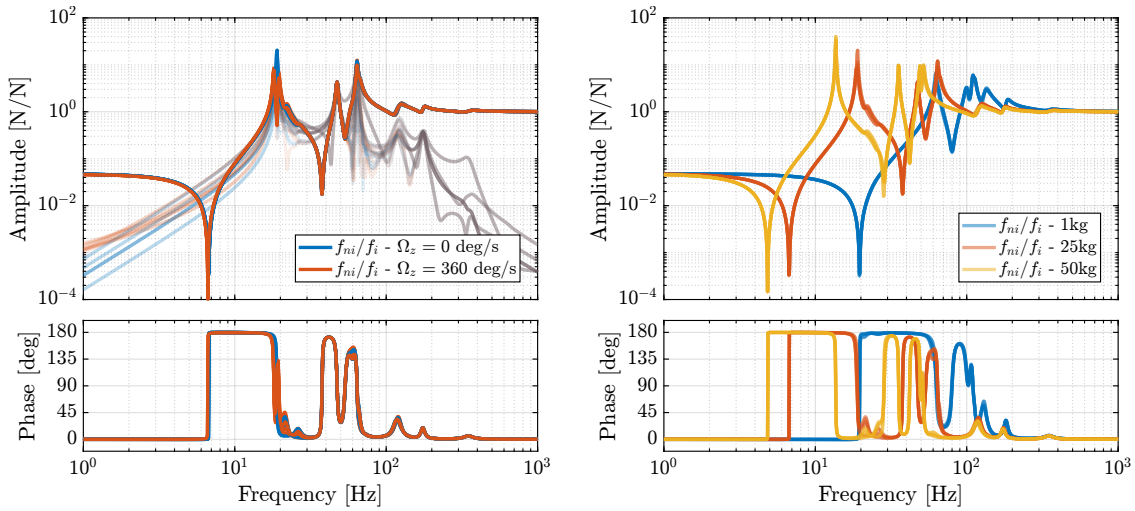

(a) Effect of Spindle rotation

(b) Effect of payload mass

Figure 3.2: Effect of the Spindle's rotational velocity on the IFF plant (a) and effect of the payload's mass on the IFF plant (b)

using pure integrators, this would results in high loop gain at low frequencies, adversely affecting the damped plant dynamics, which is undesirable. To resolve this issue, a second-order high-pass filter is introduced to limit the low frequency gain, as shown in Equation (3.1).

$$\boldsymbol{K}_{\text{IFF}}(s) = g \cdot \begin{bmatrix} K_{\text{IFF}}(s) & & 0 \\ & \ddots & \\ 0 & & K_{\text{IFF}}(s) \end{bmatrix}, \quad K_{\text{IFF}}(s) = \frac{1}{s} \cdot \frac{\frac{s^2}{\omega_z^2}}{\frac{s^2}{\omega_z^2} + 2\xi_z \frac{s}{\omega_z} + 1} \tag{3.1}$$

The cut-off frequency of the second-order high-pass filter is tuned to be below the frequency of the complex conjugate zero for the highest mass, which is at 5 Hz. The overall gain is then increased to have large loop gain around resonances to be damped, as illustrated in Figure 3.3.

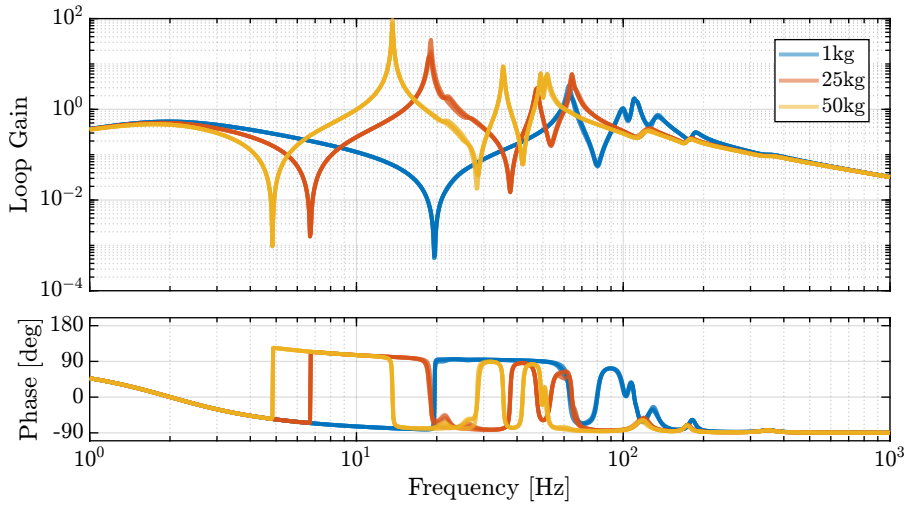

Figure 3.3: Loop gain for the decentralized IFF: $K_{\text{IFF}}(s) \cdot \frac{f_{mi}}{f_i}(s)$

To verify stability, root loci for the three payload configurations are computed and shown in Figure 3.4. The results demonstrate that the closed-loop poles remain within the left-half plane, indicating the robust stability properties of the applied decentralized IFF.

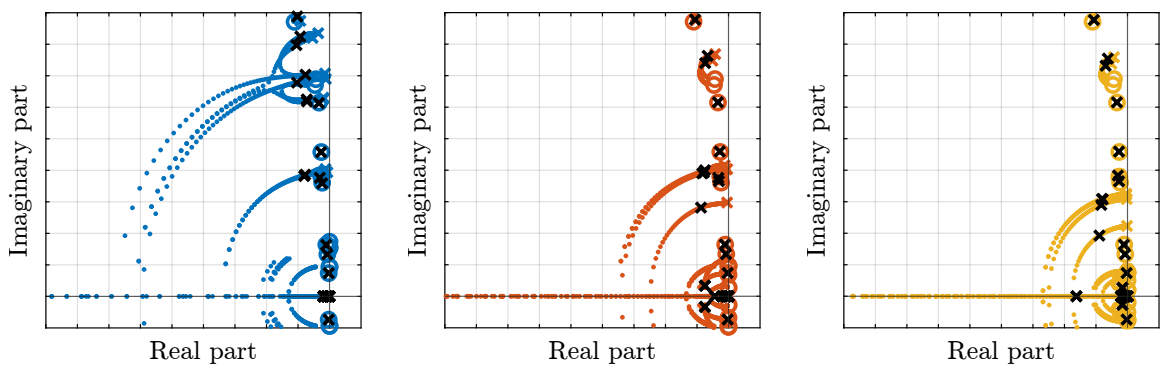

(a) 1 kg **(b)** 25 kg **(c)** 50 kg

Figure 3.4: Root Loci for Decentralized IFF for three payload masses. Closed-loop poles are shown by the black crosses.

4 Centralized Active Vibration Control

The implementation of high-bandwidth position control for the nano-hexapod presents several technical challenges. The plant dynamics exhibit complex behavior influenced by multiple factors including payload mass, rotational velocity, and the mechanical coupling between the nano-hexapod and the micro-station. This section presents the development and validation of a centralized control strategy designed to achieve precise sample positioning during high-speed tomography experiments.

First, a comprehensive analysis of the plant dynamics is conducted in Section 4.1, examining the effects of spindle rotation, payload mass variation, and the implementation of Integral Force Feedback (IFF). Section 4.2 validates previous modeling predictions that both overly stiff and overly compliant nano-hexapod configurations lead to degraded performance, through detailed analysis using the multi-body model. Building upon these findings, Section 4.3 presents the design of a robust high-authority controller capable of maintaining stability across varying payload masses while achieving the desired control bandwidth.

The performance of the developed control strategy is validated through simulations of tomography experiments in Section 4.4. These simulations incorporate realistic disturbance sources and evaluate system performance against the stringent positioning requirements imposed by future beamline specifications. Particular attention is paid to the system's behavior under maximum rotational velocity conditions and its ability to accommodate varying payload masses, demonstrating the practical viability of the proposed control approach.

4.1 HAC Plant

The plant dynamics from force inputs $\boldsymbol{f}$ to the strut errors $\boldsymbol{\epsilon}_{\mathcal{L}}$ were first extracted from the multi-body model without implementation of the decentralized IFF. The influence of spindle rotation on plant dynamics was investigated, with results presented in Figure 4.1a. While rotational motion introduces coupling effects at low frequencies, these remain minimal at operational velocities, owing to the high stiffness characteristics of the nano-hexapod assembly.

Payload mass emerged as a significant parameter affecting system behavior, as illustrated in Figure 4.1b. As expected, increasing payload mass was found to decrease resonance frequencies while amplifying coupling at low frequency. These mass-dependent dynamic changes present considerable challenges for control system design, particularly for configurations with high payload masses.

Additional operational parameters were systematically evaluated, including the R_y tilt angle, R_z spindle position, and micro-hexapod position. These factors were found to exert negligible influence on the plant dynamics, attributable to the effective mechanical decoupling achieved between the plant and micro-station dynamics. This decoupling characteristic ensures consistent performance across various operational configurations. This also validates the developed control kinematics.

The Decentralized Integral Force Feedback was implemented in the multi-body model, and transfer

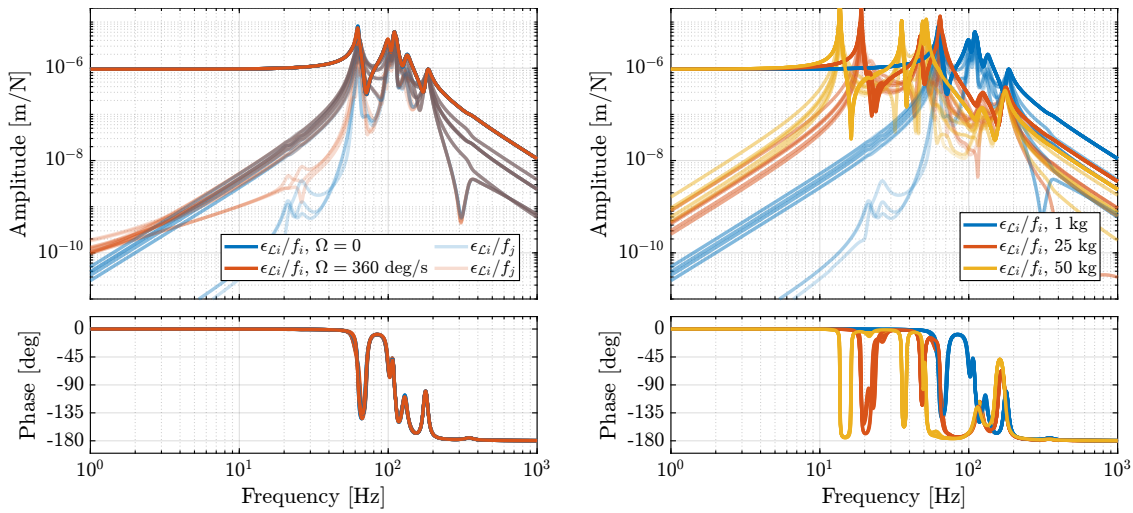

(a) Effect of rotational velocity Ω_z

(b) Effect of payload's mass

Figure 4.1: Effect of the Spindle's rotational velocity on the positioning plant (a) and effect of the payload's mass on the positioning plant (b)

functions from force inputs $\boldsymbol{f}'$ of the damped plant to the strut errors $\boldsymbol{\epsilon}_{\mathcal{L}}$ were extracted from this model.

The effectiveness of IFF implementation was first evaluated with a 1 kg payload, as demonstrated in Figure 4.2a. The results indicate successful damping of the nano-hexapod resonance modes, though a minor increase in low-frequency coupling was observed. This trade-off was considered acceptable given the overall improvement in system behavior.

The benefits of IFF implementation were further assessed across the full range of payload configurations, with results presented in Figure 4.2b. For all tested payloads (1 kg, 25 kg and 50 kg), decentralized IFF significantly damped the nano-hexapod modes and therefore simplified the system dynamics. More importantly, is the fact that in the vicinity of the wanted high authority control bandwidth (i.e. between 10 Hz and 50 Hz), the damped dynamics (shown in red) exhibited minimal gain and phase variations with frequency. For the undamped system (shown in blue), achieving robust control with bandwidth above 10Hz while maintaining stability across different payload masses would be practically unfeasible.

The coupling between the nano-hexapod and micro-station was evaluated through comparative analysis of plant dynamics under two mounting conditions. In the first configuration, the nano-hexapod was mounted on an ideally rigid support, while in the second configuration, it was installed on the micro-station with finite compliance.

As illustrated in Figure 4.3, the complex dynamics of the micro-station were found to have little impact on the plant dynamics. The only observable difference manifests as alternating poles and zeros above 100Hz, a frequency range sufficiently beyond the control bandwidth to avoid interference with system performance. This finding confirms effective dynamic decoupling between the nano-hexapod and the supporting micro-station structure.

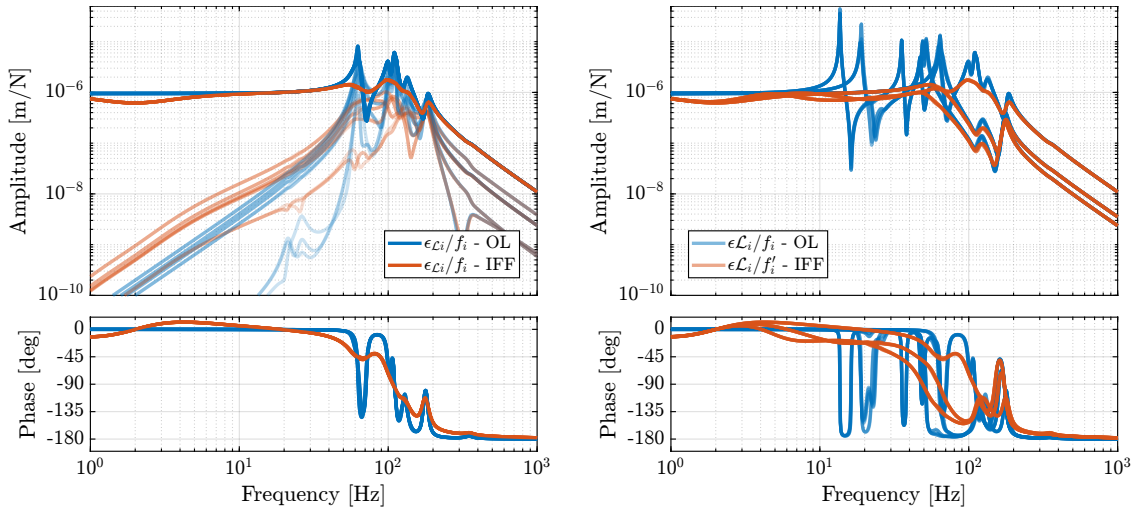

(a) Effect of IFF - $m = 1\,\text{kg}$

(b) Effect of IFF on the set of plants to control

Figure 4.2: Effect of Decentralized Integral Force Feedback on the positioning plant for a 1 kg sample mass (a). Direct terms of the positioning plants for all considered payloads are shown in (b).

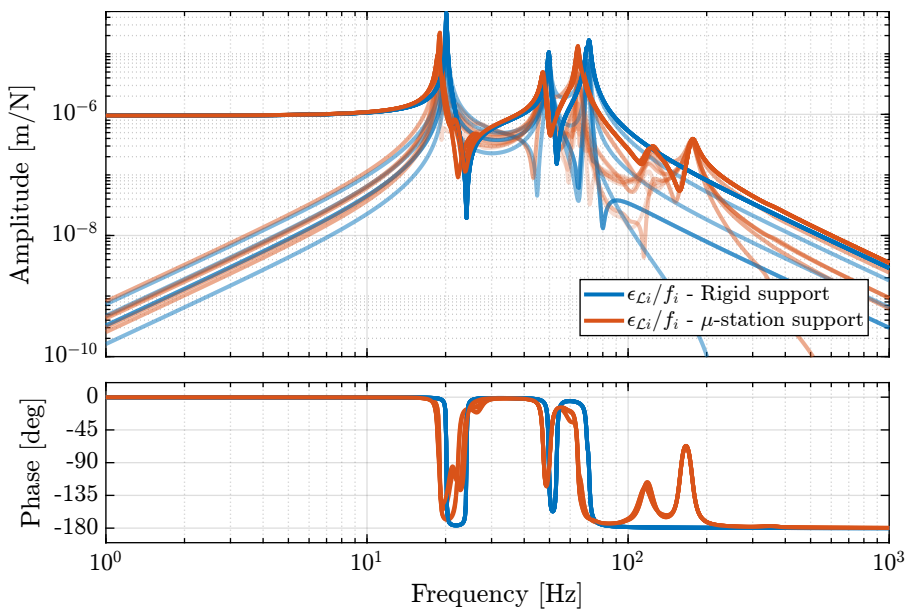

Figure 4.3: Effect of the micro-station limited compliance on the plant dynamics

4.2 Effect of Nano-Hexapod Stiffness on System Dynamics

The influence of nano-hexapod stiffness was investigated to validate earlier findings from simplified uniaxial and three-degree-of-freedom (3DoF) models. These models suggested that a moderate stiffness of approximately $1\,N/\mu m$ would provide better performance compared to either very stiff or very soft configurations.

For the stiff nano-hexapod analysis, a system with actuator stiffness of $100\,N/\mu m$ was simulated with a 25 kg payload. The transfer function from $\boldsymbol{f}$ to $\boldsymbol{\epsilon}_{\mathcal{L}}$ was evaluated under two conditions: mounting on an infinitely rigid base and mounting on the micro-station. As shown in Figure 4.4a, significant coupling was observed between the nano-hexapod and micro-station dynamics. This coupling introduces complex behavior that proves difficult to model and predict accurately, corroborating the predictions of the simplified uniaxial model.

The soft nano-hexapod configuration was evaluated using a stiffness of $0.01\,N/\mu m$ with a 25 kg payload. Dynamic response was characterized at three rotational velocities: 0, 36, and 360 deg/s. Figure 4.4b demonstrates that rotation substantially impacts system dynamics, manifesting as instability at high rotational velocities, increased coupling from gyroscopic effects, and rotation-dependent resonance frequencies. The current approach of controlling the motion in the strut frame proves inadequate for soft nano-hexapods; but even shifting control to the payload's center of mass frame would not overcome the substantial coupling and dynamic variations induced by gyroscopic effects.

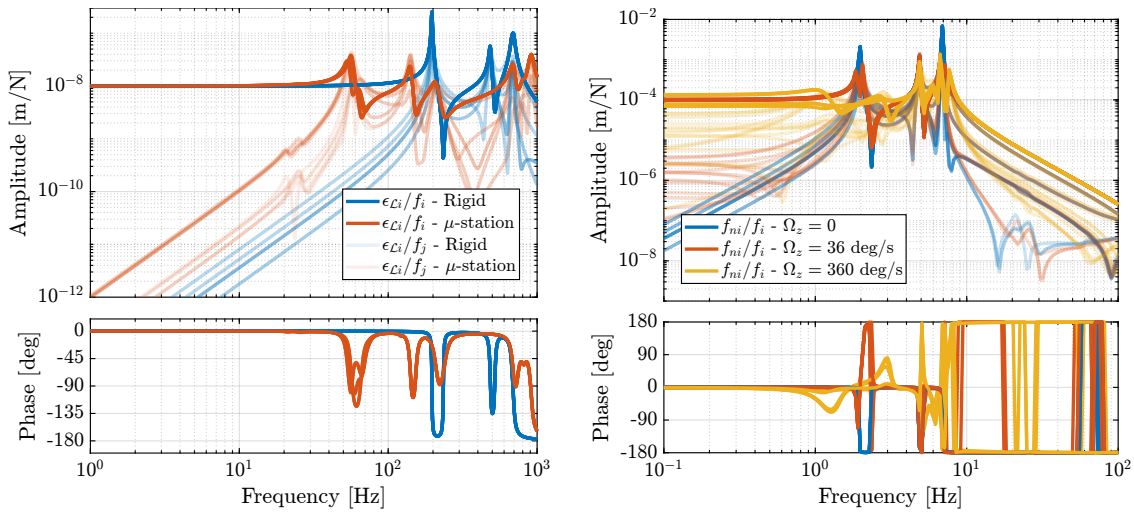

(a) $k_a = 100\,N/\mu m$ - Coupling with the micro-station **(b)** $k_a = 0.01\,N/\mu m$ - Effect of Spindle rotation

Figure 4.4: Coupling between a stiff nano-hexapod ($k_a = 100\,N/\mu m$) and the micro-station (a). Large effect of the spindle rotational velocity for a compliance ($k_a = 0.01\,N/\mu m$) nano-hexapod (b)

4.3 Controller design

A high authority controller was designed to meet two key requirements: stable for all payload masses (i.e. for all the damped plants of Figure 4.2b), and achievement of sufficient bandwidth (targeted at 10Hz)

for high performance operation. The controller structure is defined in Equation (4.1), incorporating an integrator term for low frequency performance, a lead compensator for phase margin improvement, and a low-pass filter for robustness against high frequency modes.

$$K_{\mathrm{HAC}}(s) = g_0 \cdot \underbrace{\frac{\omega_c}{s}}_{\text{int}} \cdot \underbrace{\frac{1}{\sqrt{\alpha}} \frac{1 + \frac{s}{\omega_c/\sqrt{\alpha}}}{1 + \frac{s}{\omega_c\sqrt{\alpha}}}}_{\text{lead}} \cdot \underbrace{\frac{1}{1 + \frac{s}{\omega_0}}}_{\text{LPF}}, \quad (\omega_c = 2\pi 10\,\mathrm{rad/s},\ \alpha = 2,\ \omega_0 = 2\pi 80\,\mathrm{rad/s}) \tag{4.1}$$

The controller's performance was evaluated through two complementary analyses. First, the decentralized loop gain, shown in Figure 4.5a, confirms the achievement of the desired 10Hz bandwidth. Second, the characteristic loci analysis presented in Figure 4.5b demonstrates robustness for all payload masses, with adequate stability margins maintained throughout the operating envelope.

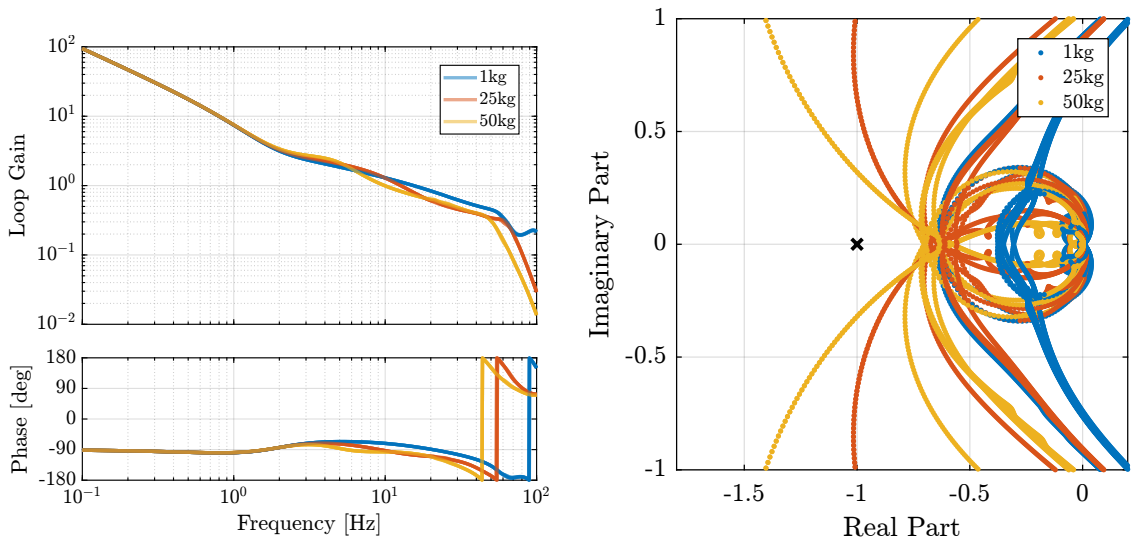

(a) Loop Gain

(b) Characteristic Loci

Figure 4.5: High Authority Controller - "Diagonal Loop Gain" (a) and Characteristic Loci (b)

4.4 Tomography experiment

The Nano Active Stabilization System concept was validated through time-domain simulations of scientific experiments, with particular focus on tomography scanning due to its demanding performance requirements. Simulations were conducted at the maximum operational rotational velocity of $\Omega_z = 360\,\mathrm{deg/s}$ to evaluate system performance under the most challenging conditions.

Performance metrics were established based on anticipated future beamline specifications, which specify a beam size of 200nm (horizontal) × 100nm (vertical). The primary requirement stipulates that the point of interest must remain within these beam dimensions throughout operation. The simulation incorporated two principal disturbance sources: ground motion and spindle vibrations. Additional noise sources, including measurement noise and electrical noise from DAC and voltage amplifiers, were not included in this analysis as these parameters will be optimized during the detailed design phase.

Figure 4.6 presents a comparative analysis of positioning errors under both open-loop and closed-loop conditions for a lightweight sample configuration (1kg). The results demonstrate the system's capability to maintain position within the specified beam dimensions, validating the fundamental concept of the stabilization system.

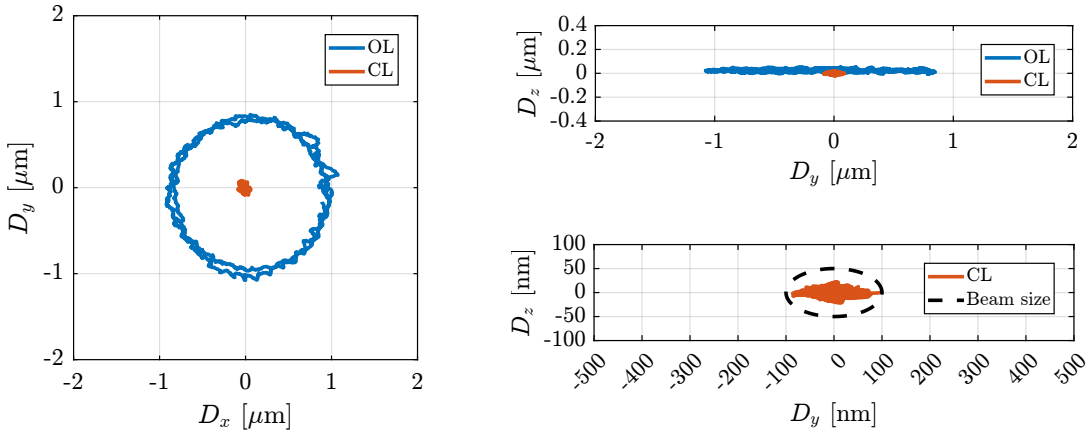

(a) XY plane

(b) YZ plane

Figure 4.6: Position error of the sample in the XY (a) and YZ (b) planes during a simulation of a tomography experiment at 360 deg/s. 1kg payload is placed on top of the nano-hexapod.

The robustness of the NASS to payload mass variation was evaluated through additional tomography scan simulations with 25kg and 50kg payloads, complementing the initial 1kg test case. As illustrated in Figure 4.7, system performance exhibits some degradation with increasing payload mass, aligning with predictions from the control analysis. While the positioning accuracy for heavier payloads is outside the specified limits, it remains within acceptable bounds for typical operating conditions.

It should be noted that the maximum rotational velocity of 360deg/s is primarily intended for lightweight payload applications. For higher mass configurations, rotational velocities are foreseen to be below 36deg/s.

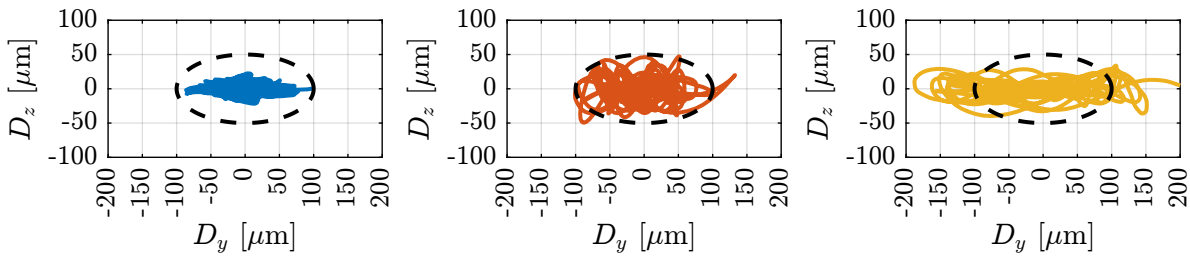

(a) $m = 1\,kg$

(b) $m = 25\,kg$

(c) $m = 50\,kg$

Figure 4.7: Simulation of tomography experiments - 360deg/s. Beam size shown by dashed black

Conclusion

The development and analysis presented in this chapter have successfully validated the Nano Active Stabilization System concept, marking the completion of the conceptual design phase. A comprehensive control strategy has been established, effectively combining external metrology with nano-hexapod sensor measurements to achieve precise position control. The implementation follows the proven High Authority Control - Low Authority Control architecture, which has been successfully adapted for this specific application.

The decentralized Integral Force Feedback component has been demonstrated to provide robust active damping across various operating conditions. The addition of parallel springs to the force sensors, has been shown to ensure stability during spindle rotation. The centralized High Authority Controller, operating in the frame of the struts for simplicity, has achieved the desired performance objectives. This investigation has confirmed that the moderate actuator stiffness of 1 $N/\mu m$ represents an adequate choice for the nano-hexapod, as both very stiff and very compliant configurations have been shown to introduce significant performance limitations.

The control system has achieved the targeted bandwidth of 10 Hz while maintaining robustness to payload mass variations. These theoretical predictions have been validated through simulations of tomography experiments, where positioning accuracy requirements were defined by the expected minimum beam dimensions of 200 nm $\times$ 100 nm. The system has demonstrated excellent performance at maximum rotational velocity with lightweight samples. While some degradation in positioning accuracy has been observed with heavier payloads, as anticipated by the control analysis, the overall performance remains sufficient to validate the fundamental concept of the NASS.

These results provide a solid foundation for advancing to the subsequent detailed design phase and experimental implementation.

Bibliography

[1] A. Preumont, B. De Marneffe, and S. Krenk, "Transmission zeros in structural control with collocated multi-input/multi-output pairs," *Journal of guidance, control, and dynamics*, vol. 31, no. 2, pp. 428–432, 2008 (cit. on p. 7).